

Highly anisotropic hybridization, dispersion, damping, and propagation of quantum plasmons in graphene superlattices

Yuan Cao,^{1,2} Xiaoguang Li,^{3,2,*} Dongli Wang,¹ Xiaodong Fan,¹ Xiaobo Lu,¹ Zhenyuan Zhang,¹
Changgan Zeng,^{1,2,4,†} and Zhenyu Zhang^{2,4}

¹*Hefei National Laboratory for Physical Sciences at the Microscale (HFNL) and Department of Physics, University of Science and Technology of China, Hefei, Anhui, 230026, China*

²*International Center for Quantum Design of Functional Materials (ICQD), HFNL, University of Science and Technology of China, Hefei, Anhui, 230026, China*

³*Shenzhen Institutes of Advanced Technology, Chinese Academy of Sciences, Shenzhen, Guangdong 518055, China*

⁴*Synergetic Innovation Center for Quantum Information and Quantum Physics, University of Science and Technology of China, Hefei, Anhui, 230026, China*

(Received 28 September 2014; revised manuscript received 18 November 2014; published 9 December 2014)

Graphene superlattices have been extensively investigated and exhibit various emergent single-particle properties in addition to those of pristine graphene, yet to date, the collective plasmonic behaviors of the Dirac electrons in such systems remain largely unexplored. Here we use a microscopic description to explore the quantum plasmonic properties of one-dimensional graphene superlattices under physically realistic conditions. The emerging additional Dirac points at nonzero electron energies caused by the chiral nature of graphene carriers lead to interband excitations between the induced minibands. Such segments of the electron-hole pair continuum are strongly coupled to the plasmon modes along the superlattice direction. As a result, there exist a spectrum of emergent quantum plasmonic effects, including enhanced damping, multiple plasmon modes at the same wave vector, and oscillatory plasmon energies with respect to the sweeping Fermi level. In contrast, the coupling along the perpendicular direction is much weaker, and the plasmonic dispersion and damping remain largely intact as those of pristine graphene. These findings of fundamental nature may also offer additional technological potentials in graphene optoelectronics, such as plasmonic waveguides.

DOI: [10.1103/PhysRevB.90.245415](https://doi.org/10.1103/PhysRevB.90.245415)

PACS number(s): 73.22.Pr, 73.20.Mf, 73.21.Cd

I. INTRODUCTION

Graphene has attracted a great amount of research interest [1,2] due to its unique linear energy dispersion $E_k = \pm v_F |\mathbf{k}|$, where $v_F = c/300$ is the group velocity in graphene (c is the vacuum light speed) [3]. Such massless Dirac fermion behavior distinguishes graphene from conventional two-dimensional (2D) massive electron systems with parabolic energy dispersion, as reflected by a spectrum of unusual properties [4]. When graphene is subject to a periodic potential, more intriguing quantum effects emerge in addition to those of pristine graphene. Recently theoretical studies have highlighted anisotropy in the band structure [5] and generation of additional Dirac points [5,6] and these band modifications further lead to unconventional degeneracy and step size in the quantum Hall conductivity [7]. Other extraordinary behaviors for such graphene superlattices have also been predicted, including emerging zero modes [7–9], effective magnetic fields [10], and gap opening induced by electron interactions [11]. Experimentally, generation of additional Dirac points has been confirmed by adopting the moiré superlattices in graphene coupled to hexagonal boron nitride [12]. More recently, such moiré superlattice systems have been observed to exhibit Hofstadter's butterfly pattern in quantum transport measurements [13–15].

Besides the single-particle properties, the plasmonic behaviors of pristine graphene have also been studied, and are

found to differ substantially from those in conventional metals and semiconductors [16–30]. Examples include the unusual plasmon energy (ω_p)–carrier density (n) relationship [16–20] ($n^{1/4}$, in contrast to the $n^{1/2}$ dependence in conventional 2D electron systems [31]), plasmon-electron coupling [21], composite excitations [22,23], strong and tunable plasmon-light coupling [19,24,25], long lifetime [26], and effective confinement [26–28]. Nevertheless, despite the intriguing single-particle phenomena revealed in graphene superlattices, their collective plasmonic behaviors still remain largely unexplored. Since the collective motion is inherently related to the single-particle behaviors [16], it is conceptually intriguing to see if strong modulations of the plasmonic properties in the quantum regime should also be present in graphene superlattices.

Earlier studies have shown that the graphene-mediated plasmon modes can be largely tuned by a periodic dielectric environment [32,33], while here we discuss an intrinsic tunability based on the modulation of the electronic ground states in the graphene sheet. In this work, we investigate the quantum plasmonic modes of graphene subject to a one-dimensional Kronig-Penney periodic potential using a microscopic description. The generated Dirac points modify the electron-hole pair continuum in pristine graphene into successive emerging segments. Such continuum segments are in turn coupled strongly to the plasmon modes along the superlattice direction, but only coupled very weakly to that along the normal direction. These highly anisotropic couplings give rise to the strong anisotropic plasmonic behaviors with exotic richness.

*lixg@siat.ac.cn

†cgzeng@ustc.edu.cn

II. METHODS

Here we consider a symmetric square periodic potential applied to an infinite 2D graphene sheet as shown in Fig. 1(a). The period of this superlattice is a and the amplitude of the square potential is V . The direction along the superlattice is defined as x and the perpendicular direction is defined as y . Since the particle-hole symmetry is still retained in such a superlattice, we will consider only $E_F > 0$ in this work. Near the corner point K of the first Brillouin zone (BZ), the effective Hamiltonian of graphene at low energy can be expressed as

$$H_0 = v_F \begin{pmatrix} 0 & k_x - ik_y \\ k_x + ik_y & 0 \end{pmatrix}, \quad (1)$$

where k_x and k_y are the momenta along x and y directions, respectively, measured from the K point. Within a superlattice potential, the Hamiltonian becomes

$$H = H_0 + V_{\text{ext}}(x), \quad (2)$$

where

$$V_{\text{ext}}(x) = \begin{cases} -\frac{V}{2}, & na < x \leq (n + \frac{1}{2})a, \\ \frac{V}{2}, & (n + \frac{1}{2})a < x \leq (n + 1)a. \end{cases} \quad (3)$$

The band dispersion and eigenstates of such a Hamiltonian are obtained by treating V_{ext} as a weak perturbation and then numerically evaluating the Hamiltonian matrix using a planar-wave basis [5]. The Hamiltonian matrix elements are

$$\langle ks | H | k's' \rangle = \langle ks | H_0 | k's' \rangle + \sum_{\mathbf{G}} V_{\mathbf{G}} \delta_{\mathbf{k}-\mathbf{k}', \mathbf{G}} \delta_{s,s'}, \quad (4)$$

where $s, s' = \pm 1$ stand for pseudospins and $V_{\mathbf{G}}$ are the Fourier components of $V_{\text{ext}}(x)$ at reciprocal lattice vector \mathbf{G} . Each

band is considered to be fourfold degenerate, accounting for the spins and valleys.

Figures 1(b) and 1(c) plot the miniband structures of the graphene superlattices for two different V 's in the superlattice BZ (SBZ) with $-\pi/a < k_x < \pi/a$. The additional emerged Dirac points can be found at energies $E = m\pi v_F/a$ on the $k_y = 0$ plane, where $m = \pm 1, \pm 2$, etc. Their wave vectors are located at $\mathbf{k} = (0, 0)$ when m is even and $\mathbf{k} = (\pm\pi/a, 0)$ when m is odd [5,6]. Apart from these fixed-position Dirac cones on the $k_y = 0$ plane, extra cones with linear dispersion emerge in pairs on the $k_x = 0$ plane when V is sufficiently large [7–10]. These movable extra cones are qualitatively different from those fixed Dirac points [7], but still have a nontrivial effect on the plasmonic behaviors. The fixed-position added Dirac points are inherent to the chirality of the carriers in graphene [5] and the label m can be viewed as the label of a series of minibands, each of which intersects with the minibands above and below it only at the additional emerged Dirac points. As we will demonstrate in the following sections, the single-particle transitions between these minibands play a critical role in determining the plasmonic properties of the graphene superlattices.

The plasmon frequency is solved for within the framework of the random phase approximation (RPA) subsequently [16–18,21]. The dielectric function within the RPA can be expressed as

$$\epsilon_{\text{RPA}}(\mathbf{q}, \omega) = \epsilon_r - v(\mathbf{q})\Pi(\mathbf{q}, \omega), \quad (5)$$

where $v(\mathbf{q}) = 2\pi e^2/q$ is the Fourier transform of the Coulomb interaction and $\Pi(\mathbf{q}, \omega)$ is the RPA polarizability, which can be calculated as [16,34]

$$\Pi(\mathbf{q}, \omega) = -\frac{4}{(2\pi)^2} \sum_{j,j'} \int_{\text{BZ}} d\mathbf{k} \frac{f(\epsilon_j(\mathbf{k} + \mathbf{q})) - f(\epsilon_j(\mathbf{k}))}{\omega - (\epsilon_j(\mathbf{k} + \mathbf{q}) - \epsilon_j(\mathbf{k})) + i\eta} \times |\langle \mathbf{k}, j | e^{-i\mathbf{q} \cdot \mathbf{x}} | \mathbf{k} + \mathbf{q}, j' \rangle|^2, \quad (6)$$

where \mathbf{k} integrates over the SBZ and j, j' sum over all bands independently.

The dielectric function $\epsilon_{\text{RPA}}(\mathbf{q}, \omega)$ is numerically evaluated for any given \mathbf{q} using a method based on Hilbert transformation [34]. In order to make the dielectric function appear smoother, the single-particle excitations being summed up first get broadened (~ 0.002 eV) by a rectangular function [34]. We will consider only the $T = 0$ situation such that the Fermi distribution $f(\epsilon) = \{1 + \exp[(\epsilon - E_F)/k_B T]\}^{-1}$ simplifies to step function $\theta(\epsilon - E_F)$. The Fermi energy is shifted away from the intrinsic Dirac point due to the external potential, and therefore we discuss the so-called “extrinsic plasmons,” which would not disappear at $T = 0$ [35]. The dielectric constant ϵ_r in Eq. (5) is set to 2 to emulate a graphene sheet placed onto silicon dioxide ($\epsilon_r = 4$) in vacuum.

The plasmon frequency and its decaying behavior are determined by

$$\epsilon_{\text{RPA}}(\mathbf{q}, \omega) = 0. \quad (7)$$

We adapted the method introduced in Ref. [18] to calculate the plasmon frequency and decaying behavior separately. The real part of Eq. (7) is used to obtain the plasmon frequency $\omega_p = \omega_p(\mathbf{q})$, and the decaying behavior can then be extracted from the imaginary part of $\epsilon_{\text{RPA}}(\mathbf{q}, \omega_p)$ for this particular plasmon

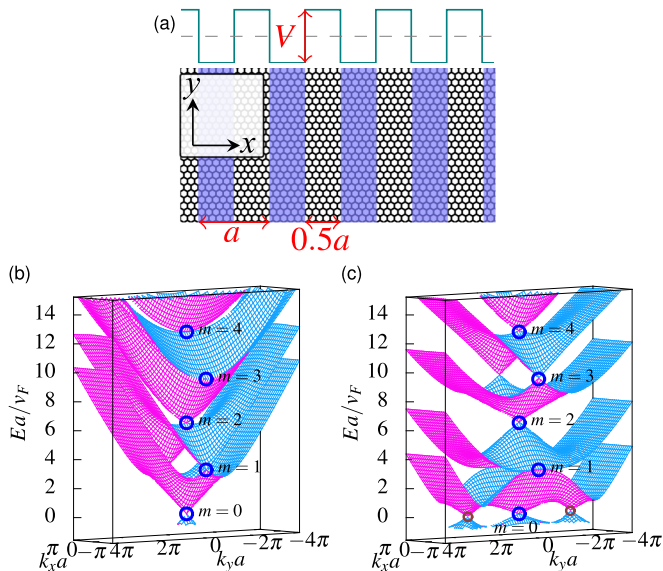


FIG. 1. (Color online) (a) Schematic of a graphene superlattice. (b),(c) Band dispersions of graphene superlattices at (b) $V = 2\pi v_F/a$ and (c) $V = 6\pi v_F/a$ (only $E \geq 0$ are displayed). Dispersion along k_x is limited in the SBZ. The large blue circles in (b) and (c) denote the Dirac points on the $k_y = 0$ plane, while the small brown circles in (c) denote the zero-energy Dirac points that exist only when $V > 4\pi v_F/a$.

mode. For example, the imaginary part of the effective wave number that accounts for decay along the direction of \mathbf{q} can be expressed as [18]

$$q_2 = \frac{\text{Im}[\Pi(q, \omega_p(q))]}{\frac{\partial}{\partial \omega} \text{Re}[\Pi(q, \omega_p(q))] \hat{q} \cdot \frac{d\omega_p}{dq}}. \quad (8)$$

In this study, we have ignored the plasmon damping induced by the electron-impurity, electron-phonon, and higher-order electron-electron interaction beyond the RPA [36]. However, as we will see later, based on our calculation, the anisotropic effect of the plasmon is prominent such that we can still expect a visible effect even if those damping processes are considered.

III. RESULTS

A. Dielectric function

1. Dispersion and E_F dependence

Figure 2 compares the dielectric functions of pristine graphene and a graphene superlattice as functions of \mathbf{q} and ω , where \mathbf{q} can be along either the x or y direction. The plasmon modes develop at the positions where the real parts of the dielectric functions are zero. The imaginary part, containing information about the single-particle excitations, characterizes the magnitude of the Landau damping of the plasmon modes [16,17]. In pristine graphene, the plasmon frequency grows monotonically with \mathbf{q} and extends into the single-particle electron-hole continuum, namely, the interband region consisting of single-particle excitations between the conduction and valence bands, where the Landau damping of the plasmon mode becomes substantially strong [16–18].

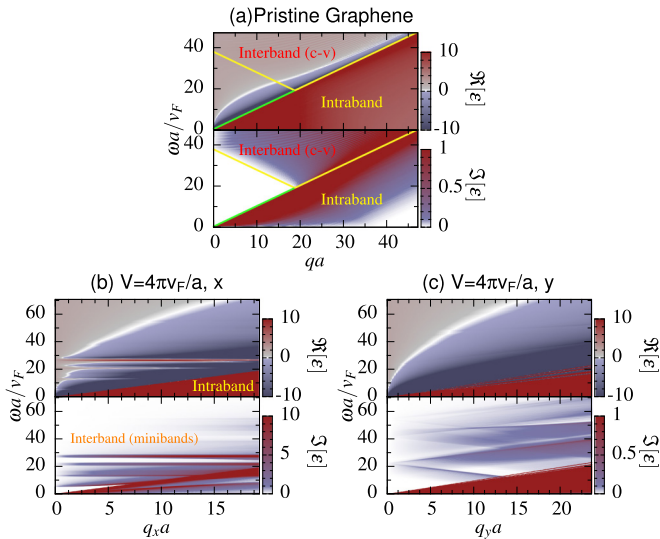


FIG. 2. (Color online) Dispersion and damping of plasmon modes in a graphene superlattice. (a) The complex dielectric function $\varepsilon(\omega, \mathbf{q})$ of pristine graphene. The plasmon modes are located at the positions where the real part of ε passes zero (represented by white color). The interband region in pristine graphene corresponds to excitations from valence band to conducting band (c-v). (b), (c) Same as (a), but in a graphene superlattice with $V = 4\pi v_F/a$ and \mathbf{q} along the (b) x and (c) y directions. E_F is $6\pi v_F/a$ for all three panels.

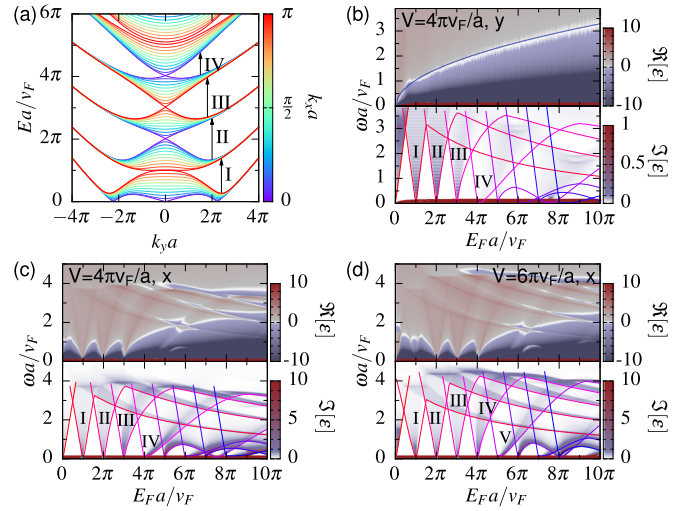


FIG. 3. (Color online) Effect of interband excitations on the dielectric functions. (a) Illustration of interband excitations between different minibands labeled with roman numbers. (b)–(d) The real and imaginary parts of the dielectric functions, at (b) $V = 4\pi v_F/a$ along the y direction, at (c) $V = 4\pi v_F/a$ along the x direction, and at (d) $V = 6\pi v_F/a$ along the x direction. All calculations assume $|\mathbf{q}| = 0.05\pi/a$. The dashed line in the upper panel of (b) depicts the plasmon energies of pristine graphene. The dashed lines in the lower panels of (b)–(d) depict the lowest energies for each type of interband excitation labeled in (a). Note that the scales for the imaginary parts in (b) and (c), (d) are different.

Unlike pristine graphene, which has a continuous conic dispersion, a graphene superlattice has a miniband structure and interband excitations between the minibands [see Fig. 3(a)] have more significant influence on the frequency and damping of the plasmon modes. The interaction between the plasmon modes and interband single-particle modes will broaden the plasmon modes by introducing extra Landau damping, and will also hybridize the dispersion of these excitons, leading to the complex dispersion relationship shown in Fig. 2(b). As a consequence of the hybridization, there can exist more than one plasmon mode at the same \mathbf{q} value. This phenomenon could be analogized to various composite excitations in which the miniband structure is obtained by quantum confinement [37]. Interestingly, the strong hybridization occurs only along the x direction. The plasmon modes along the y direction are coupled much less strongly with the single-particle excitation regions, and their energy dispersions largely resemble that of pristine graphene.

Next, we show the dependence of the plasmon modes on the Fermi energy E_F by plotting the dielectric function against E_F and ω in Fig. 3. The plasmon frequencies are still at the roots of the real part of the dielectric function. From these figures, “ribbonlike” shapes are noticed, in which the large imaginary part of the dielectric function implies relatively strong Landau damping. These ribbons clearly outline the region of the interband excitations. In Fig. 3, we have also plotted the E_F dependence of the lower limits of the interband transition energies across different miniband band gaps [38]. Due to the strong coupling between the plasmon and interband single-particle modes, the plasmon modes along the x direction

tend to avoid overlapping with the ribbonlike regions, thus providing the oscillating energy curves as shown in Figs. 3(c) and 3(d). The behaviors of the plasmon energy curves are rather complicated at large E_F , due to the intersections with multiple ribbons. In contrast, the y -direction plasmon energy basically preserves the simple $\omega_p \sim E_F^{1/2}$ relationship as in pristine graphene [Fig. 3(b)], again thanks to the considerably weaker interaction with the interband excitations along the y direction.

2. Effect of movable Dirac cones

We have mentioned that when V is sufficient large, extra Dirac points emerge in pairs from the set of immobile Dirac points. This happens not only to the original Dirac point of graphene at $E = 0$ which has been studied as extra zero modes in Refs. [7–10], but also to Dirac points corresponding to $m \neq 0$ under larger V . The previously studied additional zero modes can lead to oscillating behavior in conductivity [8,9] and higher degeneracy of Landau levels [7]. From the viewpoint of plasmonic behavior, these extra Dirac cones (not limited to zero energy) can result in relatively stronger Landau damping at low energy and further modify the plasmon frequency.

It has been shown that in a superlattice the ratio v_y/v_x of the group velocities, which characterizes the anisotropy near a Dirac point, can reach zero if provided with some specific values of V [6]. In fact, for our simplified case of a square potential, the ratio at the m th fixed Dirac point can be written analytically as

$$\left(\frac{v_y}{v_x}\right)_m = \frac{2v}{\pi(v^2 - m^2)} \begin{cases} \sin \frac{\pi v}{2}, & m = 2n, \\ \cos \frac{\pi v}{2}, & m = 2n + 1, \end{cases} \quad (9)$$

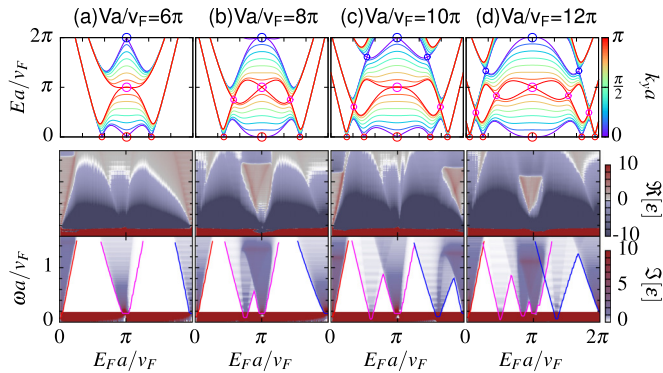


FIG. 4. (Color online) The miniband structures and dielectric functions of a graphene superlattice near the energy $E = \pi v_F/a$, with superlattice potential amplitude $V =$ (a) $6\pi v_F/a$, (b) $8\pi v_F/a$, (c) $10\pi v_F/a$, and (d) $12\pi v_F/a$. In the uppermost panel of each panel, fixed Dirac points (large circles) and movable Dirac points (small circles) are labeled in the miniband structure. Since all movable Dirac points are split from the fixed Dirac points in the center, Dirac points originating from the same Dirac point are labeled in the same color, and each of the colors corresponds to one curve in the lowermost panel, which stands for the lowest possible energy for the corresponding interband transition.

where $v = \frac{|V|a}{2\pi v_F}$. The first few of these functions are plotted in Fig. 5(a) as solid lines with maximum values $(v_y/v_x)_{\max} = 1$. It is generally observed that, for any m as V increases, this ratio will first rise to 1 (except at $m = 0$), and drop to 0 at a multiple of $2\pi v_F/a$; after that it will bounce up and repeat this variation. From Eq. (9), v_y drops to zero when

$$|V|_m = (m + 2l) \frac{2\pi v_F}{a}, \quad l = 1, 2, \dots \quad (10)$$

At these well-defined values of V , additional mobile Dirac points spawn from the fixed Dirac points in pairs [39]. The upper panels of Figs. 4(a)–4(d) illustrate the continuous generation of additional Dirac points as V increases.

The mobile Dirac points not only move away from the original Dirac point in k space, but also move towards lower

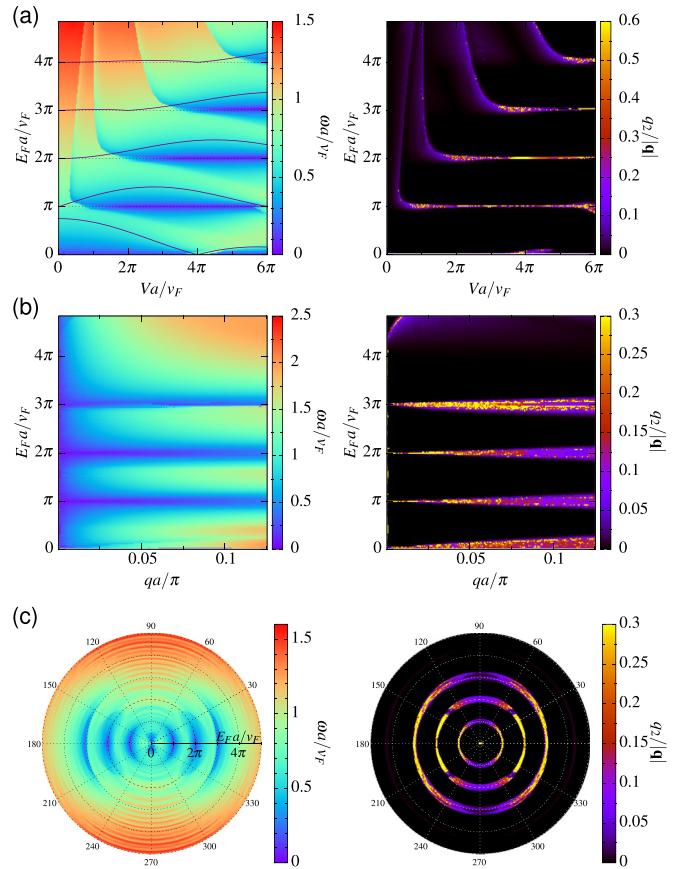


FIG. 5. (Color online) Various mappings of the plasmon energy and damping of a graphene superlattice. (a) E_F - V mapping of the x -direction plasmon energy and damping. $q_x = 0.02\pi/a$ and $q_y = 0$ in this calculation. The superimposed curves depict the ratio of band group velocity $|v_y/v_x|$ as a function of V near different Dirac points. These curves are vertically shifted to the energies of the corresponding Dirac points for clarification. (b) E_F - q_x mapping of the x -direction plasmon energy and damping. $V = 4\pi v_F/a$ in this calculation. (c) Polar mapping of the plasmon energy and damping with respect to E_F and angle of \mathbf{q} . $|\mathbf{q}|$ is fixed to $0.02\pi/a$. The tiny fringes on the plasmon energy mapping are caused by limited k -space discretization, which should be neglected. For (a)–(c), in the cases where multiple plasmon frequencies exist at the same point, the one with lowest energy is always chosen.

energies. In the corresponding plots of dielectric functions in Fig. 4, the fan-shaped regions split into multiple subregions, the number of which equals the number of different transition energies between the Dirac points. The plasmon frequency adds further complications on top of the original oscillating behavior, and leads to a second oscillation with respect to V .

B. Plasmon energy

The interband ribbons together with the plasmon energy evolve with increasing V in a complex manner (see the video in the Supplemental Material [40]), in association with the band structure of the graphene superlattice. It is generally observed that as V grows, the ribbons tend to be narrowed and gather higher intensity. Consequently, a ribbon with higher intensity is able to create a significant drop in the x -direction plasmon energy curve [For example, compare the ribbon labeled as IV in Figs. 3(c) and 3(d).]. Along the y direction, the strength of the Landau damping is still determined by their intensity, although the intensities of the ribbons are not enough to substantially affect the plasmon dispersion.

Figure 5 displays the plasmon energy and damping as functions of different system parameters. In order to gain more quantitative insights into the effect of plasmon damping, q_2 that has been described in Eq. (8) is calculated to give a rough estimate of the number of wavelengths for the plasmon mode can possibly propagate before it decays exponentially [18]. As shown in Fig. 5(a), the valleys seen at the energies of the Dirac points $E_F = m\pi v_F/a$ are the signatures of the narrowed ribbons that we have discussed above. As V increases, the number of the valleys also increases. On the other hand, the valleys disappear at values of V specified by Eq. (10). Intriguingly, we see a clear correspondence between the ratio $|v_y/v_x|$ defined in Eq. (9) and the depth of the valley of the same Dirac point: a higher v_y/v_x results in a deeper valley at the corresponding energy. This fact further supports the point that a close correlation holds between the plasmon modes and the miniband structure of the graphene superlattices. Aside from V and E_F , the energy and damping of the plasmon modes in the graphene superlattices also exhibit strong tunability on the magnitude and direction of \mathbf{q} , as shown in Figs. 5(b) and 5(c). Essentially, the plasmon shows the strongest decay along the x direction as E_F is set around the Dirac points. This strong and controllable anisotropy in the plasmon propagation

provides a further possibility for plasmonic applications in graphene superlattices, such as highly directional plasmonic waveguides [30,41].

IV. SUMMARY AND CONCLUSION

Recently, graphene superlattices with periods down to several tens of nanometers have been achieved by adopting nanofabrication [42,43]. Such small period ensures carrier dynamics to be in the quantum regime. Therefore, the rich quantum plasmonic behaviors described above in graphene superlattices can feasibly be observed. The plasmon modes in a graphene superlattice can be excited by electromagnetic radiation if the graphene ribbons are adopted to fulfill a wave vector match [19]. Assuming a superlattice period $a = 50$ nm and a ribbon width $L = 0.5$ μm , the emergence of the second lowest valley as shown in Fig. 5(a) requires $V > 20$ meV and the position of the valley will be $E_F = 41$ meV. These values are within the limit of current technologies [42,43]. The typical plasmon energy in this circumstance will be ~ 3 THz, lying in the range for terahertz applications.

In conclusion, we have investigated the quantum plasmonic behaviors of one-dimensional graphene superlattices. The emerging additional Dirac points due to the chiral nature of graphene modify the band structures into a series of minibands. The induced electron-hole pair continua are coupled strongly to the plasmon modes along the superlattice direction, and this leads to multiple hybridized plasmon modes at the same wave vector, enhanced damping, and oscillatory plasmon frequency with respect to the sweeping Fermi level. In contrast, the plasmonic behaviors along the perpendicular direction are barely affected by these interminiband excitations. These rich plasmonic properties may shed light onto the exploration of graphene-based electromagnetic and optoelectronic devices, for instance plasmonic waveguides and filters.

ACKNOWLEDGMENTS

This work was supported in part by the NSFC (Grants No. 11434009, No. 11374279, and No. 11034006), NKBRPC (Grant No. 2014CB921102), CAS (Grant No. XDB01020000), SRFDP (Grant No. 20113402110046), and FRFCU (Grants No. WK2340000011 and No. WK2340000035).

-
- [1] K. S. Novoselov, A. K. Geim, S. V. Morozov, D. Jiang, M. I. Katsnelson, I. V. Grigorieva, S. V. Dubonos, and A. A. Firsov, *Nature (London)* **438**, 197 (2005).
 - [2] Y. Zhang, Y.-W. Tan, H. L. Stormer, and P. Kim, *Nature (London)* **438**, 201 (2005).
 - [3] In this work, we use natural units where $c = \hbar = 1$. For electrostatic quantities, Gaussian units are used, so that the potential of an electron is $V(r) = -e/r$.
 - [4] A. H. Castro Neto, F. Guinea, N. M. R. Peres, K. S. Novoselov, and A. K. Geim, *Rev. Mod. Phys.* **81**, 109 (2009).
 - [5] C.-H. Park, L. Yang, Y.-W. Son, M. L. Cohen, and S. G. Louie, *Nat. Phys.* **4**, 213 (2008).
 - [6] C.-H. Park, L. Yang, Y.-W. Son, M. L. Cohen, and S. G. Louie, *Phys. Rev. Lett.* **101**, 126804 (2008).
 - [7] C.-H. Park, Y.-W. Son, L. Yang, M. L. Cohen, and S. G. Louie, *Phys. Rev. Lett.* **103**, 046808 (2009).
 - [8] L. Brey and H. A. Fertig, *Phys. Rev. Lett.* **103**, 046809 (2009).
 - [9] M. Barbier, P. Vasilopoulos, and F. M. Peeters, *Phys. Rev. B* **81**, 075438 (2010).
 - [10] J. Sun, H. A. Fertig, and L. Brey, *Phys. Rev. Lett.* **105**, 156801 (2010).
 - [11] J. C. W. Song, A. V. Shytov, and L. S. Levitov, *Phys. Rev. Lett.* **111**, 266801 (2013).

- [12] M. Yankowitz, J. Xue, D. Cormode, J. D. Sanchez-Yamagishi, K. Watanabe, T. Taniguchi, P. Jarillo-Herrero, P. Jacquod, and B. J. LeRoy, *Nat. Phys.* **8**, 382 (2012).
- [13] C. R. Dean, L. Wang, P. Maher, C. Forsythe, F. Ghahari, Y. Gao, J. Katoch, M. Ishigami, P. Moon, M. Koshino, T. Taniguchi, K. Watanabe, K. L. Shepard, J. Hone, and P. Kim, *Nature (London)* **497**, 598 (2013).
- [14] B. Hunt, J. D. Sanchez-Yamagishi, A. F. Young, M. Yankowitz, B. J. LeRoy, K. Watanabe, T. Taniguchi, P. Moon, M. Koshino, P. Jarillo-Herrero, and R. C. Ashoori, *Science* **340**, 1427 (2013).
- [15] L. A. Ponomarenko, R. V. Gorbachev, G. L. Yu, D. C. Elias, R. Jalil, A. A. Patel, A. Mishchenko, A. S. Mayorov, C. R. Woods, J. R. Wallbank, M. Mucha-Kruczynski, B. A. Piot, M. Potemski, I. V. Grigorieva, K. S. Novoselov, F. Guinea, V. I. Fal'ko, and A. K. Geim, *Nature (London)* **497**, 594 (2013).
- [16] E. H. Hwang and S. Das Sarma, *Phys. Rev. B* **75**, 205418 (2007).
- [17] B. Wunsch, T. Stauber, F. Sols, and F. Guinea, *New J. Phys.* **8**, 318 (2006).
- [18] M. Jablan, H. Buljan, and M. Soljačić, *Phys. Rev. B* **80**, 245435 (2009).
- [19] L. Ju, B. Geng, J. Horng, C. Girit, M. Martin, Z. Hao, H. A. Bechtel, X. Liang, A. Zettl, Y. R. Shen, and F. Wang, *Nat. Nanotechnol.* **6**, 630 (2011).
- [20] H. Yan, T. Low, W. Zhu, Y. Wu, M. Freitag, X. Li, F. Guinea, P. Avouris, and F. Xia, *Nat. Photon.* **7**, 394 (2013).
- [21] M. Polini, R. Asgari, G. Borghi, Y. Barlas, T. Pereg-Barnea, and A. H. MacDonald, *Phys. Rev. B* **77**, 081411(R) (2008).
- [22] A. Bostwick, F. Speck, T. Seyller, K. Horn, M. Polini, R. Asgari, A. H. MacDonald, and E. Rotenberg, *Science* **328**, 999 (2010).
- [23] M. Freitag, T. Low, W. Zhu, H. Yan, F. Xia, and P. Avouris, *Nat. Commun.* **4**, 1951 (2013).
- [24] F. H. L. Koppens, D. E. Chang, and F. J. García de Abajo, *Nano Lett.* **11**, 3370 (2011).
- [25] N. Kumada, S. Tanabe, H. Hibino, H. Kamata, M. Hashisaka, K. Muraki, and T. Fujisawa, *Nat. Commun.* **4**, 1363 (2013).
- [26] A. N. Grigorenko, M. Polini, and K. S. Novoselov, *Nat. Photon.* **6**, 749 (2012).
- [27] J. Chen, M. Badioli, P. Alonso-González, S. Thongrattanasiri, F. Huth, J. Osmond, M. Spasenović, A. Centeno, A. Pesquera, P. Godignon, A. Z. Elorza, N. Camara, F. J. García de Abajo, R. Hillenbrand, and F. H. L. Koppens, *Nature (London)* **487**, 77 (2012).
- [28] Z. Fei, A. S. Rodin, G. O. Andreev, W. Bao, A. S. McLeod, M. Wagner, L. M. Zhang, Z. Zhao, M. Thiemens, G. Dominguez, M. M. Fogler, A. H. Castro Neto, C. N. Lau, F. Keilmann, and D. N. Basov, *Nature (London)* **487**, 82 (2012).
- [29] Y. Liu, R. F. Willis, K. V. Emtsev, and T. Seyller, *Phys. Rev. B* **78**, 201403 (2008).
- [30] A. Vakil and N. Engheta, *Science* **332**, 1291 (2011).
- [31] S. Das Sarma and A. Madhukar, *Phys. Rev. B* **23**, 805 (1981).
- [32] N. M. R. Peres, Yu. V. Bludov, A. Ferreira, and M. I. Vasilevskiy, *J. Phys.: Condens. Matter* **25**, 125303 (2013).
- [33] I. Arrazola, R. Hillenbrand, and A. Yu. Nikitin, *Appl. Phys. Lett.* **104**, 011111 (2014).
- [34] L. Caramella, G. Onida, F. Finocchi, L. Reining, and F. Sottile, *Phys. Rev. B* **75**, 205405 (2007).
- [35] S. Das Sarma and Qiuzi Li, *Phys. Rev. B* **87**, 235418 (2013).
- [36] A. Principi, G. Vignale, M. Carrega, and M. Polini, *Phys. Rev. B* **88**, 195405 (2013).
- [37] X. Li, D. Xiao, and Z. Zhang, *New J. Phys.* **15**, 023011 (2013).
- [38] In an electron system with a Fermi level, only those processes that transition from below to above the Fermi energy are possible and have an effect on the electronic properties including plasmons. The lowest possible interband transition energy thus has a nontrivial dependence on the Fermi energy.
- [39] In fact, $l = -1, -2, -3, \dots$ also satisfies $v_y = 0$. However, additional Dirac points do not spawn at these corresponding V 's.
- [40] See Supplemental Material at <http://link.aps.org/supplemental/10.1103/PhysRevB.90.245415> for additional calculated results in video format.
- [41] J. T. Kim and S.-Y. Choi, *Opt. Express* **19**, 24 (2011).
- [42] S. Dubey, V. Singh, A. K. Bhat, P. Parikh, S. Grover, R. Sensarma, V. Tripathi, K. Sengupta, and M. M. Deshmukh, *Nano Lett.* **13**, 3990 (2013).
- [43] M. Drienovsky, F.-X. Schrettenbrunner, A. Sandner, D. Weiss, J. Eroms, M.-H. Liu, F. Tkatschenko, and K. Richter, *Phys. Rev. B* **89**, 115421 (2014).